Bifunctional Electrocatalyst Engineered via Polyanionic Synergy and Heterointerface Modulation for Robust Seawater Electrolysis

*Fang Zheng[a], Zhenhua Fang[a], Mayur A. Gaikwad[a], Suyoung Jang[a], Seyeon Cho[b], Jong Sung Park[b], Jin Hyeok Kim[a]**

* Corresponding author

[a] Optoelectronics Convergence Research Center and Department of Materials Science and Engineering, Chonnam National University, Yongbong-Dong, Buk-Gu, Gwangju 61186, South Korea

[b] Department of Energy Engineering, Gyeongsang National University, Jinju, Gyeongnam 52828, South Korea

Corresponding author E-mail address: jinhyeok@chonnam.ac.kr

1. Experimental section

1.1 Chemicals

Nickel foam (NF), cobalt(II) nitrate hexahydrate ($Co(NO_3)_2 \cdot 6H_2O$, ≥98%), nickel(II) nitrate hexahydrate ($Ni(NO_3)_2 \cdot 6H_2O$, ≥97.0%), iron(III) nitrate nonahydrate ($Fe(NO_3)_3 \cdot 9H_2O$, ≥98%), 2-methylimidazole ($C_4H_6N_2$, 99%), and thioacetamide (C_2H_5NS, 98%), ruthenium(IV) oxide (RuO_2, 99.9%), activation carbon, and N-Methyl Pyrrolidone (C_5H_9NO, ≥99.0%) were purchased form Sigma-Aldrich. All reagents did not require further purification. NF was used as a substrate, which was ultrasonically cleaned with ethanol and deionized water for 5 minutes, respectively. The seawater used in the experiment was sourced from Yeosu in South Korea.

1.2 Synthesis mechanism of ZIF-67

ZIF-67 was grown on NF via a coordinated self-assembly process. First, NF (4 × 1 cm^2) was immersed in an aqueous solution of $Co(NO_3)_2 \cdot 6H_2O$ (0.5 mmol, 0.1455 g in 10 mL DI water) for 30 min to enable electroadsorption of Co^{2+} ions onto the NF surface. Subsequently, 2-methylimidazole ($C_4H_6N_2$, 4 mmol, 0.3284 g in 10 mL DI water) was rapidly added. The ligand undergoes deprotonation ($C_4H_6N_2 \leftrightarrow C_4H_5N_2^- + H^+$) and coordinates with adsorbed Co^{2+} to form ZIF-67 nuclei [1]:

$$Co^{2+} + 2C_4H_5N_2^- \rightarrow Co(C_4H_5N_2)_2 \downarrow \text{(ZIF-67)}.$$

After 2 h of static reaction, crystalline ZIF-67 was obtained via Ostwald ripening. The product was washed with DI water and dried at 60 °C for 12 h.

1.3 Synthesis mechanism of Co-Ni_3S_2 and Ni_3S_2

Co-Ni_3S_2 was synthesized via a solvothermal reaction using ZIF-67/NF as a precursor. First, thioacetamide (TAA, 0.6 g) was dissolved in ethanol (60 mL) under stirring for 10 min. The ZIF-67/NF was then immersed in this solution and heated at 120 °C for 4 h. The formation mechanism of Co-Ni_3S_2 is shown as follows [2]:

TAA releases S^{2-} ions: $CH_3CSNH_2 + 2C_2H_5OH \rightarrow CH_3(NH_2)C(OC_2H_5)_2 + H_2S$

$H_2S \leftrightarrow S^{2-} + 2H^+$

ZIF-67 decomposition: $ZIF{-}67 \rightarrow Co^{2+} + 2C_4H_5N_2^-$

NF dissolution: $Ni(s) \rightarrow Ni^{2+} + 2e^-$

Co-sulfidation: $Co^{2+} + S^{2-} \rightarrow CoS$

Ni-sulfidation: $3Ni^{2+} + 2S^{2-} + 6e^- \rightarrow Ni_3S_2$

The resulting CoS and Ni_3S_2 form a Co-doped solid solution ($CoS + Ni_3S_2 \rightarrow Co{-}Ni_3S_2$) at 120 °C. Pure Ni_3S_2 was synthesized identically using bare NF without ZIF-67.

1.4 Synthesis mechanism of FeNi-LDH/Co-Ni_3S_2

The heterostructure was fabricated via electrochemical deposition. Using Co-Ni_3S_2/NF as the working electrode, Pt as the counter electrode, and Ag/AgCl as the reference, deposition was performed at -1.0 V in an aqueous electrolyte containing $Ni(NO_3)_2 \cdot 9H_2O$ (4 mmol) and $Fe(NO_3)_3 \cdot 9H_2O$ (1.3 mmol). The key steps are [3]:

1. Cathodic reduction of nitrate: $NO^{3-} + H_2O + 2e^- \rightarrow NO^{2-} + 2OH^-$
2. Co-precipitation of Fe^{3+}/Ni^{2+}: $Fe^{3+} + 3OH^- \rightarrow Fe(OH)_3$; $Ni^{2+} + 2OH^- \rightarrow Ni(OH)_2$; $Ni(OH)_2 + Fe(OH)_3 \rightarrow$ FeNi-LDH (layered).
3. CO_3^{2-} intercalation from dissolved CO_2: $CO_2 + 2OH^- \rightarrow CO_3^{2-}$

resulting in the crystalline LDH structure: $[Ni_{0.75}Fe_{0.25}(CO_3)_{0.125}(OH)_2 \cdot 0.38H_2O]$.

The reaction mechanism is as follows: FeNi-LDH is electrodeposited on the Co-Ni_3S_2 substrate via cathodic reduction of nitrate ions, generating localized OH^- ions. Increasing the pH triggers the coprecipitation of Fe^{3+} and Ni^{2+} ions, forming layered double hydroxide nanoflowers that are anchored to the sulfide surface. The Fe:Ni molar ratio (1:3) was controlled by ion concentration. Deposition time (15-60 min) regulated LDH thickness. For comparison, NF-loaded FeNi-LDH was also prepared in the same way.

1.5 Preparation of RuO_2 electrode

RuO_2 was coated on the NF to prepare the RuO_2 catalyst by a universal approach. A total of 6 mg RuO_2 was ultrasonically dispersed for at least 5 min in a mixture solution containing 0.16 mL of NMP and PVDP and 1 mg of Activation carbon.

1.6 Materials characterization

X-ray diffractometer (XRD): XRD was carried out on an X'Pert PRO Multi-Purpose X-Ray Diffractometer (PANalytical) using Cu Kα radiation. The test sample is a 1 cm^2 nickel foam containing a catalyst. It is mounted on a single-crystal silicon sample stage for testing. The scanning range (2θ) is typically 5° to 90°.

Raman spectroscopy: Raman spectra were studied by NRS-5100 using a 532 nm laser source. The test sample is a 1 cm^2 nickel foam containing a catalyst. This is mounted on a glass slide, and the test area is carefully selected and focused, with the measurement range of 100-1200 cm^{-1}.

Fourier Transform Infrared Spectroscopy (FT-IR): FT-IR spectra were collected on a PerkinElmer Spectrum 3 model. The test sample, a 1 cm^2 piece of catalyst-loaded nickel foam,

was placed on a test bench, ensuring direct and close contact between the target surface and the crystal probe. The measurement range was 560–4000 cm^{-1}.

Field emission scanning electron microscope (FE-SEM) and energy dispersive spectroscopy (EDS): The morphology and element distribution of the materials were tested using a field emission scanning electron microscope (JSM-7900F, JEOL, Japan) and a matching EDS (Oxford) detector. The test sample consisted of a 5 mm × 2 mm nickel foam containing a catalyst. The sample was mounted on a sample stage. Before testing, a platinum (Pt) thin film was deposited on the sample surface (deposition time: 80 s) using an ion sputtering instrument (Cressington Scientific, US, 108auto) to improve conductivity and obtain clearer images. The coated sample was mounted on an aluminum stub, and the morphology was observed at an accelerating voltage of 5 kV.

Transmission Electron Microscopy (TEM): TEM analysis was performed on a JEM-2100F (JEOL LTD). Sample preparation was as follows: nickel foam containing the catalyst was placed in a glass vial containing 2 mL of ethanol and then sonicated for approximately 3 h to form a uniform dispersion. Subsequently, a drop of the dispersion was pipetted onto a copper grid supported by an ultrathin carbon film and allowed to air dry.

X-ray Photoelectron Spectroscopy (XPS): High-Performance X-ray Photoelectron Spectroscopy (HP-XPS, K-ALPHA+) was used to characterize the elemental composition and chemical state of the catalyst. Sample preparation consisted of a 1 cm^2 nickel foam containing the catalyst placed on a conductive substrate. A dual-beam (electron/Ar^+) neutralization gun was used to compensate for charge effects. Binding energies were calibrated using the C 1s peak (284.8 eV) of surface contamination.

Fourier Transform Nuclear Magnetic Resonance Spectroscopy (FT-NMR): A 400 MHz FT-NMR spectroscopy was performed on an AVANCE III HD 400 instrument to confirm the presence of methanol electrooxidation products in the electrolyte. Test sample preparation: After the electrochemical stability test (10 mA cm^{-2}, 25 hours), a certain amount of electrolyte was mixed with an internal standard (deuterated chloroform) and transferred to a dedicated NMR tube for analysis.

In situ Raman spectroscopy: A Renishaw inVia-Qontor Raman spectrometer equipped with a 532 nm laser source was used to investigate changes in surface species during electrochemical processes. Spectra were collected in an electrochemical cell containing 1 M KOH, using nickel foam containing the catalyst as the working electrode, Pt as the counter electrode, and Ag/AgCl as the reference electrode. Polarization curves were measured at a scan rate of 0.2 mV/s within the voltage window (1.2–1.8 V vs. RHE).

Specific Surface Area (BET) Measurement: Nitrogen adsorption-desorption isotherms were measured at 77 K using an instrument such as the Micromeritics ASAP 2460 to evaluate the specific surface area and pore structure of the material. Sample preparation: 0.1 g of powder was scraped from the nickel foam. Before testing, the sample was vacuum degassed at 120 °C for 6 hours to remove surface moisture and impurities. The specific surface area was calculated using the Brunauer-Emmett-Teller (BET) method.

Gas Chromatography (GC): The gaseous product (H_2) produced during the electrochemical reaction was analyzed online using a Micro GC Fusion gas chromatograph. The electrochemical reaction was performed using a catalyst-containing nickel foam as the working electrode, 1 M KOH as the electrolyte, and a voltage of 2.5 V.

Inductively Coupled Plasma Optical Emission Spectrometry (ICP-OES): Measure the metal ion content ratio in the catalyst using an inductively coupled optical emission spectrometry (OPTIMAA 5300 DV). Sample preparation: Place the nickel foam containing the catalyst in DI water, sonicate for 1 hour, dissolve it in high-purity nitric acid, and dilute appropriately for ICP-OES analysis. Quantification is performed using an external standard method.

1.7 Electrochemical measurement

The electrochemical performance was tested at an Autolab potentiostat (CHI Instruments, USA) using a three-electrode system. The platinum electrode and Hg/HgO electrode were used as counter electrode and reference electrode, respectively, and the as-prepared materials on NF were used as the working electrode. For electrocatalytic reactions, 1 M KOH and 1 M KOH + 0.5 M methanol were employed as electrolytes, respectively. All the electrochemical experiments were carried out in an electrolyte at 25 ℃. The area of the work electrode immersed in the electrolyte is 1 × 1 cm^2. Linear sweep voltammetry (LSV) was tested at a scan rate of 1 mV s^{-1}. For the electrochemical systems, the polarization curves were not iR compensated. Convert the potential measured in this work to a reversible hydrogen electrode (RHE) according to equation E (*vs.* RHE) = E (*vs.* Hg/HgO) + 0.098 + 0.059 × pH. The overpotential (η) was calculated according to the following equation: η = E (*vs.* RHE) – 1.23 V. Electrochemical impedance spectroscopic (EIS) was carried out using a high-performance potentiostat (Zive Potentiostat/Galvanostat/EIS, Wonatech, Republic of Korea) at a bias potential of 700 mV in the frequency range of 0.1 Hz-10000 Hz. Electrochemical active surface areas (ECSAs) were calculated based on the formula: ECSAs = C_{dl}/C_s. Among them, the double-layer capacitance (C_{dl}) was obtained by cyclic voltammetry (CV), while for Ni-/Co-based catalysts, C_s is usually adopted at 0.04 mF cm^{-2}. CV was tested in the non-Faradaic region at scan rates of 20 to 100 mV s^{-1}. The prepared

electrocatalysts' long-term stability was tested using chronopotentiometry (CP) at a current density of 500 mA cm^{-2} and a measurement time of 500 or 120 h. The overall water and methanol splitting uses FeNi-LDH/Co-Ni_3S_2 as an anode and cathode.

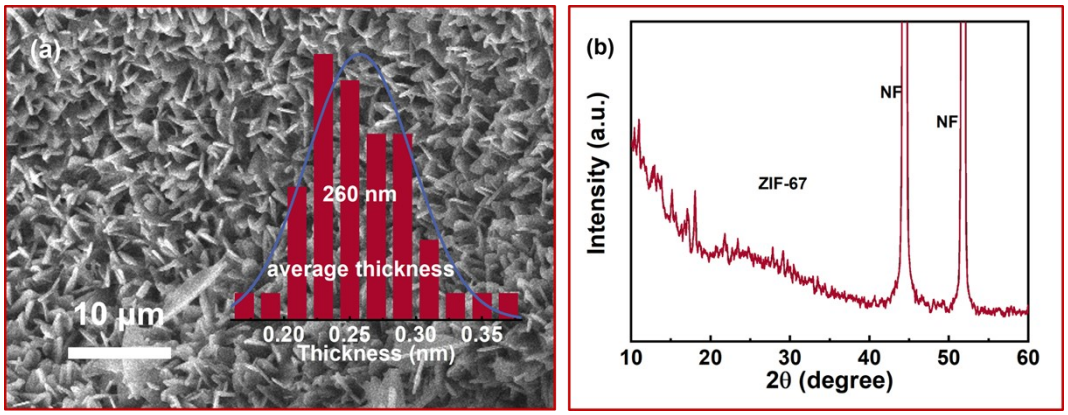

Figure S1. (a) FE-SEM image and (b) XRD pattern of ZIF-67.

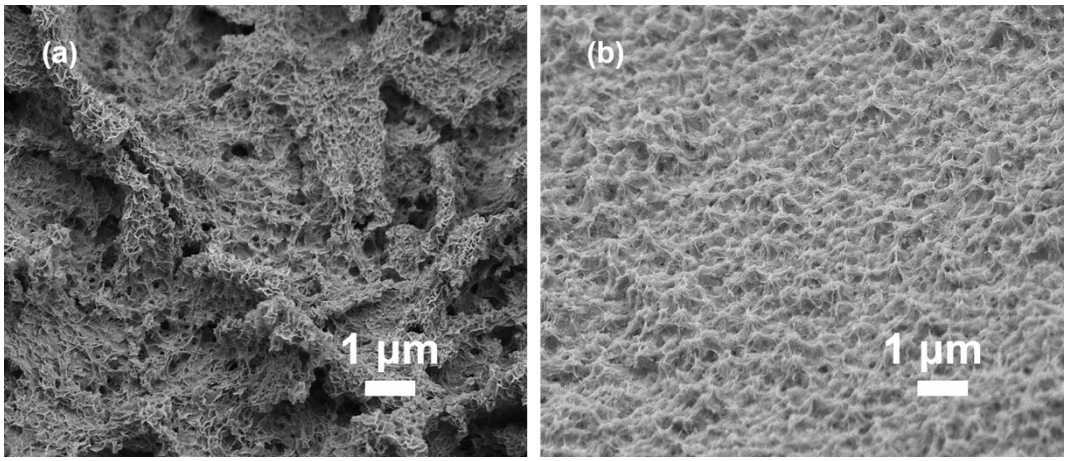

Figure S2. FE-SEM images of (a) Co-Ni_3S_2 and (b) Ni_3S_2.

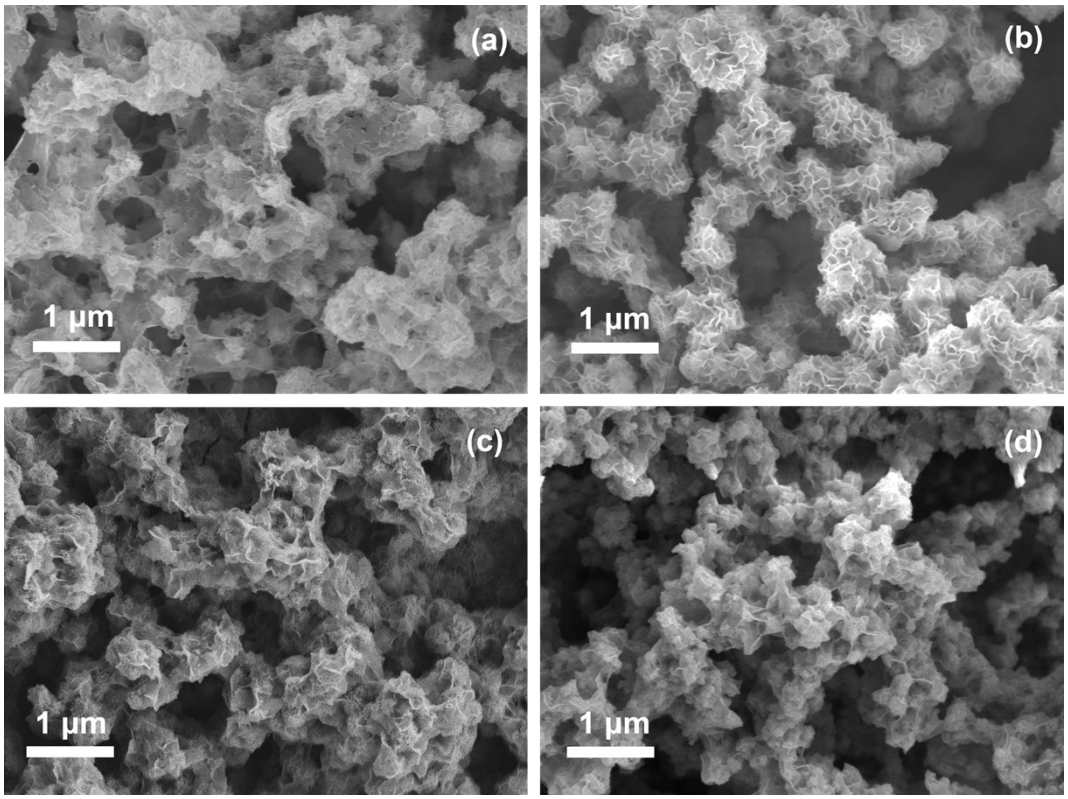

Figure S3. FE-SEM images of FeNi-LDH/Co-Ni_3S_2 with different electrodeposition times (15, 30, 45, and 60 min).

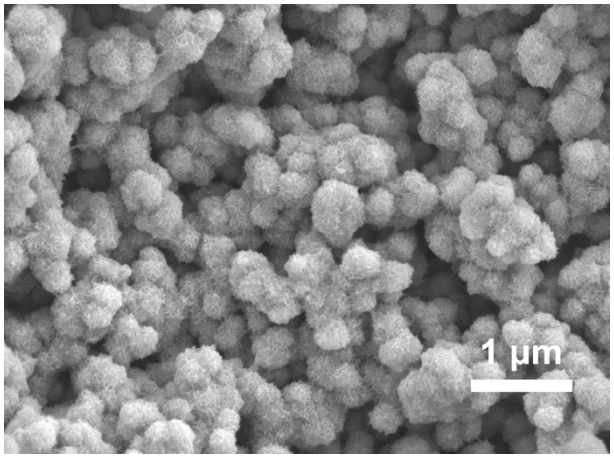

Figure S4. FE-SEM image of FeNi-LDH.

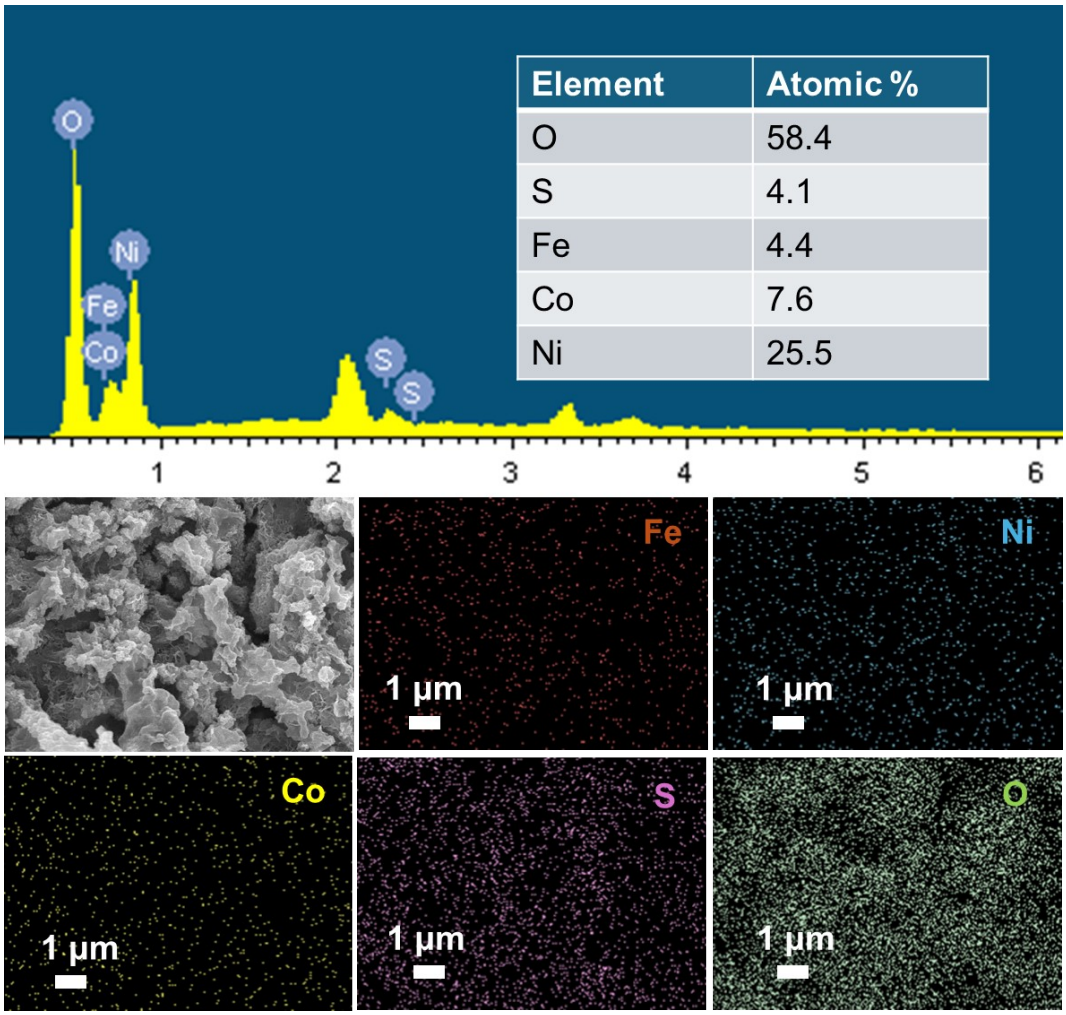

Fig. S5. EDX spectrum and element mapping of FeNi-LDH/Co-Ni_3S_2.

Table S1. Element atomic content obtained by ICP-OES analysis.

Element content / Catalyst	Fe (ppm)	Ni (ppm)	Co (ppm)
FeNi-LDH/Co-Ni_3S_2	1.59	23.11	0.61
FeNi-LDH	1.13	4.25	-
Co-Ni_3S_2	-	12.36	0.69

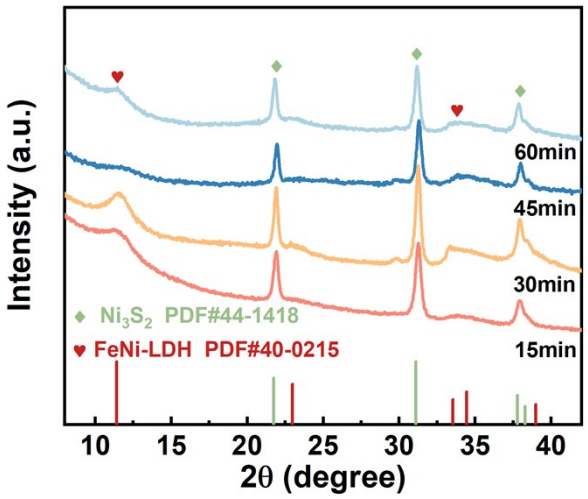

Figure S6. XRD pattern of FeNi-LDH/Co-Ni_3S_2-x with different times (x = 15, 30, 45, 60 min).

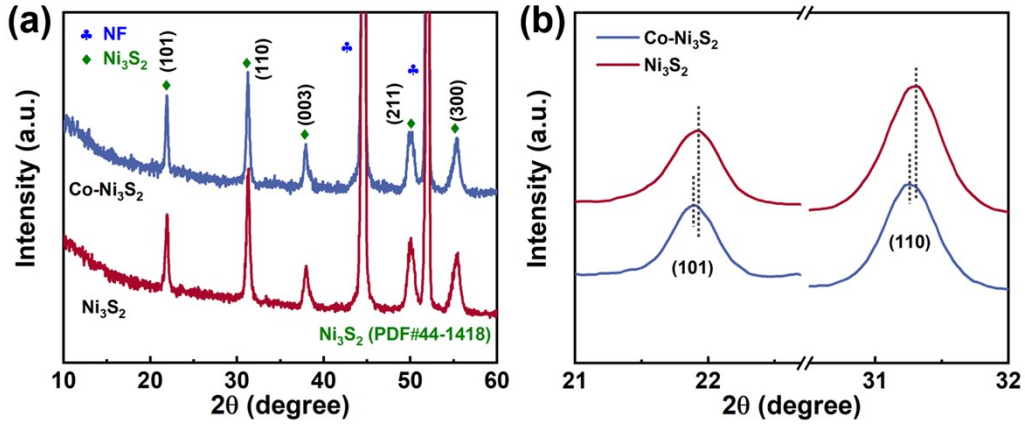

Figure S7. (a) XRD pattern of Co-Ni_3S_2 and Ni_3S_2; (b) Enlargement of partial XRD patterns of Co-Ni_3S_2 and Ni_3S_2.

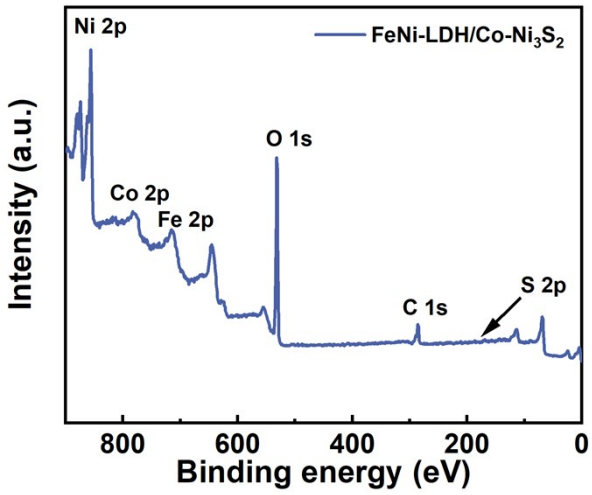

Figure S8. The XPS survey scan spectra of FeNi-LDH/Co-Ni_3S_2.

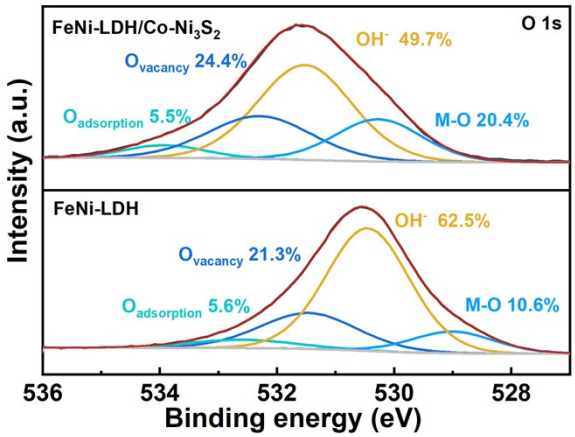

Figure S9. XPS spectra of O 1s of FeNi-LDH/Co-Ni_3S_2 and FeNi-LDH.

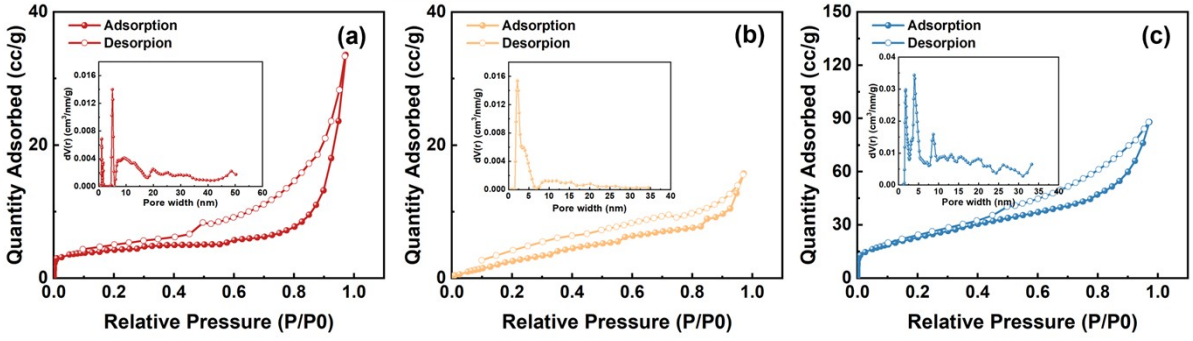

Fig. S10. Nitrogen adsorption-desorption isotherms and pore size distributions. Nitrogen adsorption-desorption isotherms and pore size distributions of (a) FeNi-LDH/Co-Ni_3S_2, (b) FeNi-LDH, and (c) Co-Ni_3S_2.

Table S2. Catalyst specific surface area and pore size values.

Catalyst	Surface area (m^2/g)	Pore size (nm)
FeNi-LDH/Co-Ni_3S_2	14.84	5.01
FeNi-LDH	13.34	2.18
Co-Ni_3S_2	84.44	3.94

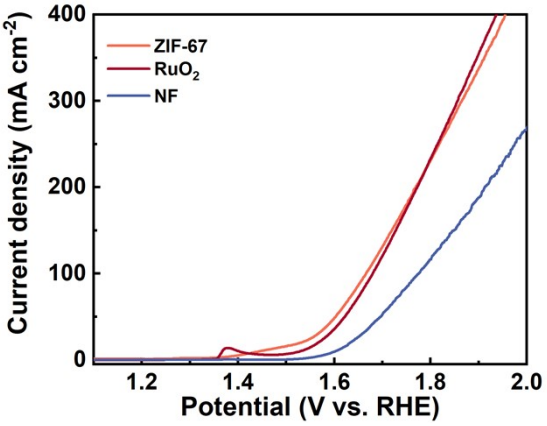

Figure S11. The LSV curves of ZIF-67, NF, and RuO_2.

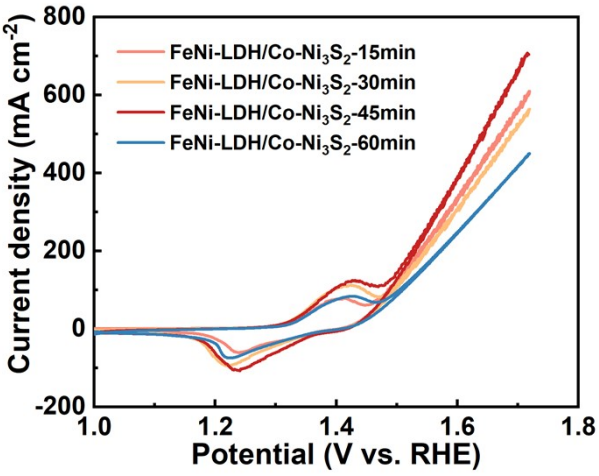

Figure S12. The CV curves of FeNi-LDH/Co-Ni_3S_2-x with different electrodeposition times (x = 15, 30, 45, and 60 min).

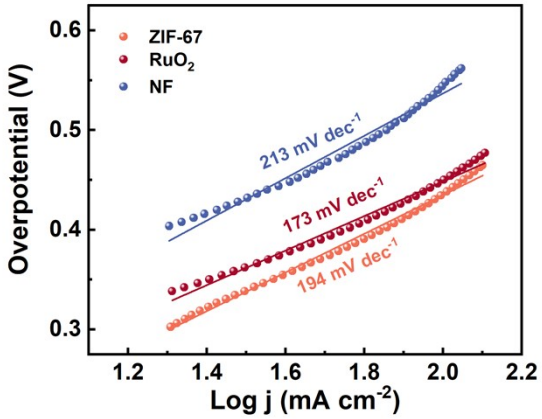

Figure S13. The corresponding Tafel slopes of ZIF-67, NF, and RuO_2.

Table. S3. Values of R_{ct} and R_s in the catalysts.

Catalyst	R_s (ohm)	R_{ct} (ohm)
FeNi-LDH/Co-Ni_3S_2	1.067	0.178
FeNi-LDH	0.977	0.182
Co-Ni_3S_2	0.936	0.742
Ni_3S_2	0.704	0.697

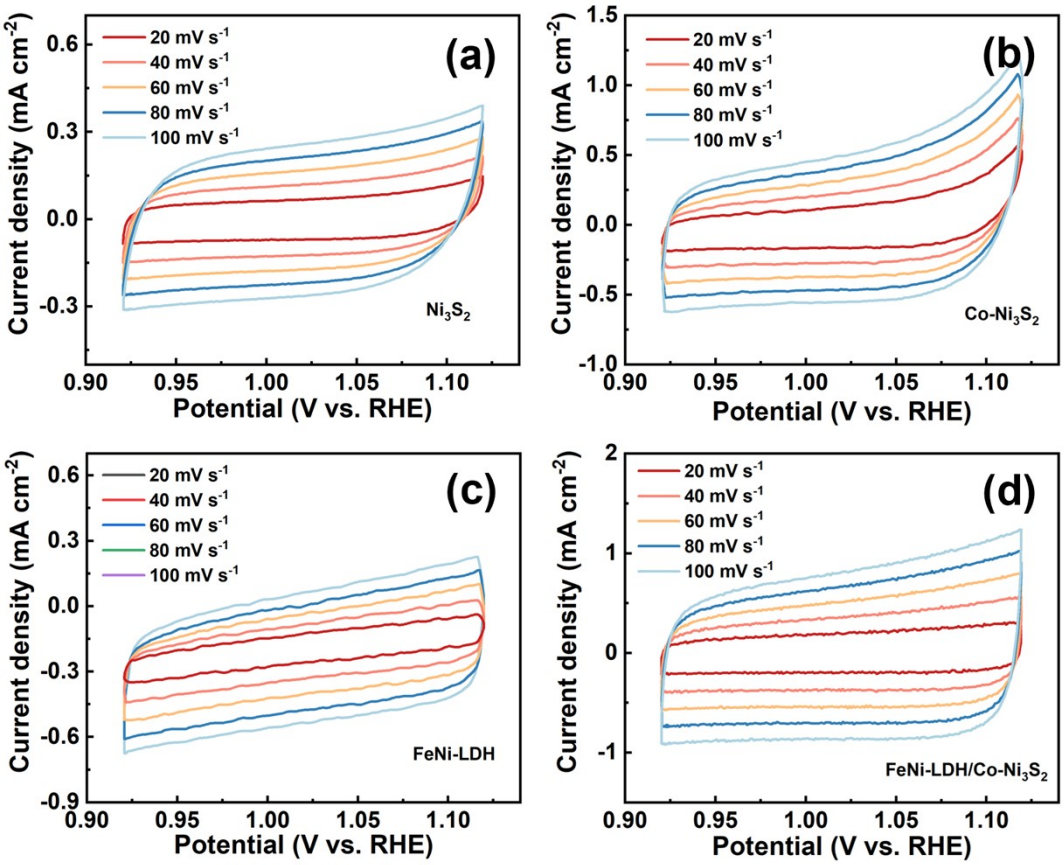

Figure S14. CV curves of (a) Ni_3S_2, (b) Co-Ni_3S_2, (c) FeNi-LDH, and (d) FeNi-LDH/Co-Ni_3S_2 at different scan rates (20-100 mV s^{-1}).

Table S4. Double-layer capacitance (C_{dl}) and electrochemical surface area (ECSA) of the catalysts in 1 M KOH.

Catalyst	C_{dl} (mF cm^{-2})	ECSA (cm^2)
FeNi-LDH/Co-Ni_3S_2	8.5	213
FeNi-LDH	3.0	75
Co-Ni_3S_2	5.0	125
Ni_3S_2	2.4	60

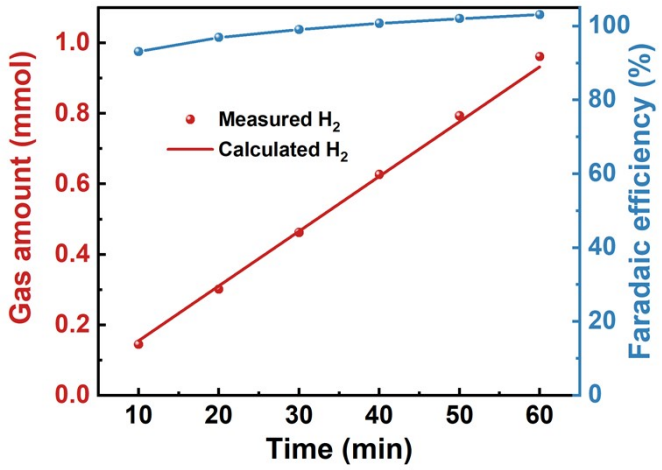

Figure S15. The Faraday efficiency of the two-electrode system in 1 M KOH.

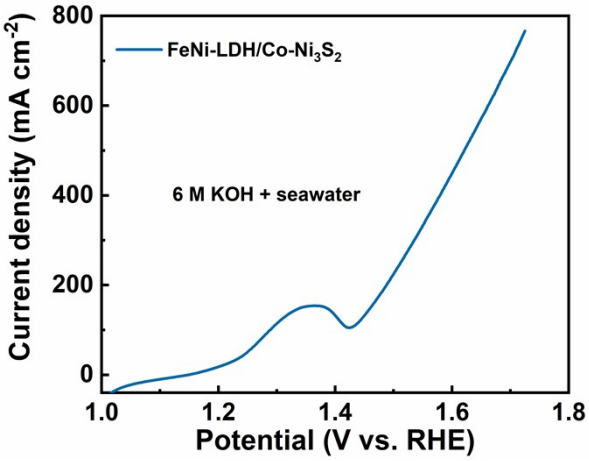

Figure S16. LSV curve of FeNi-LDH/Co-Ni_3S_2 in 6 M KOH + seawater.

Table S5. EIS and ECSA values of FeNi-LDH/Co-Ni_3S_2 in different electrolytes.

Electrolyte condition	R_s (Ω)	R_{ct} (Ω)	C_{dl} (mF cm^{-2})	ECSA (cm^2)
1 M KOH	1.07	0.18	8.5	213
1 M KOH + 1 M NaCl	0.97	0.40	8.9	223
1 M KOH + seawater	1.17	0.46	8.3	208
6 M KOH + seawater	0.53	0.10	9.9	248

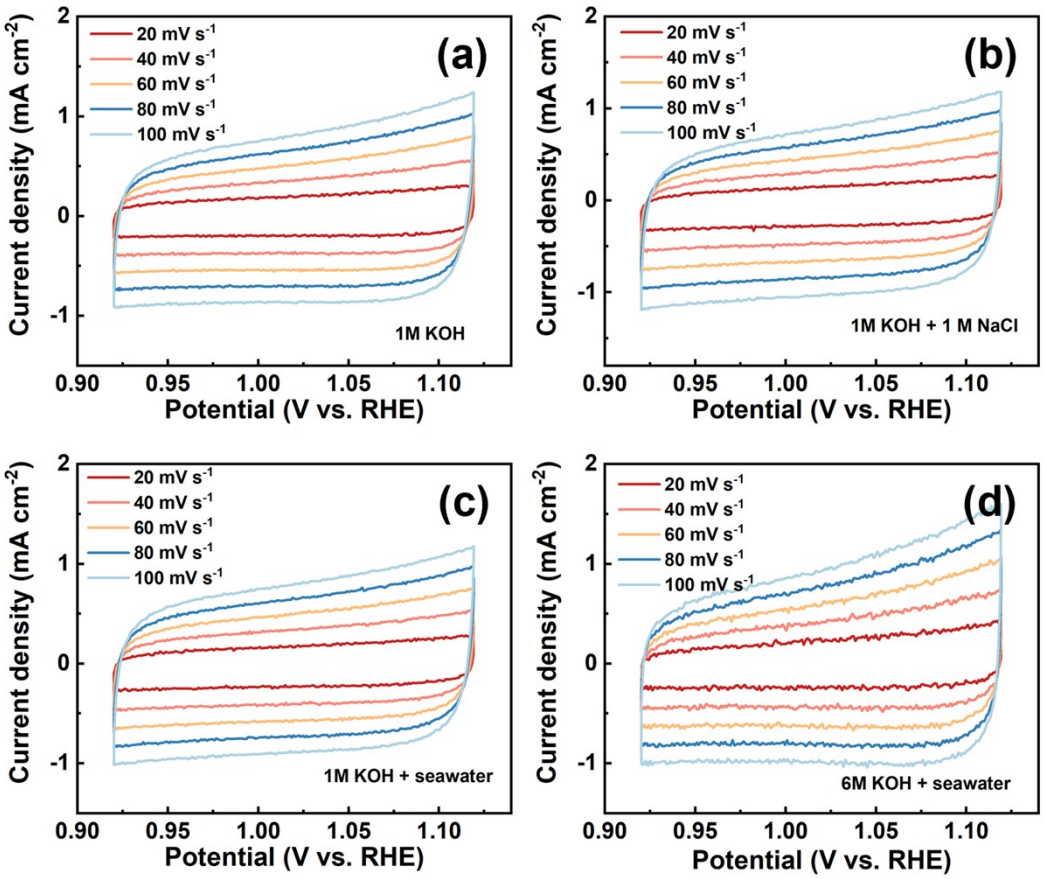

Figure S17. CV curves of FeNi-LDH/Co-Ni_3S_2 at different scan rates (20-100 mV s^{-1}) in different electrolytes. (a)1 M KOH, (b) 1 M KOH + 1 M NaCl, (c)1 M KOH + seawater, and (d) 6 M KOH + seawater.

Table S6. Comparison of OER performance between FeNi-LDH/Co-Ni_3S_2 electrocatalyst and other recently reported electrocatalysts in simulated and real alkaline seawater electrolytes.

Electrocatalysts	Overpotential (mV) @ 100 $mAcm^{-2}$	Electrolyte	Reference
FeNi-LDH/Co-Ni_3S_2	**258**	**1 M KOH + 1 M NaCl**	**This work**
	283	**1 M KOH + seawater**	
NiFe LDH/FeOOH	286	1 M KOH + 0.5 M NaCl	[4]
S-$NiMoO_4$@NiFe-LDH	315	1 M KOH + seawater	[5]
NiFe-LDH-6-4/CC	301	1 M KOH + seawater	[6]
NiFe-LDH/MOF	307	1 M KOH + seawater	[7]
Fe-Ni_3S_2	306	1 M KOH + 0.5 M NaCl	[8]
Mo-Ni_3S_2/NMF	346	1 M KOH + 0.5 M NaCl	[9]
Ni_3S_2 foam/NF	369	1 M KOH + seawater	[10]
FeMoSe@NiCo-LDH	362	1 M KOH + seawater	[11]
B-Co_2Fe LDH	310	1 M KOH + seawater	[12]
NiFe-LDH	401	1 M KOH + seawater	[13]

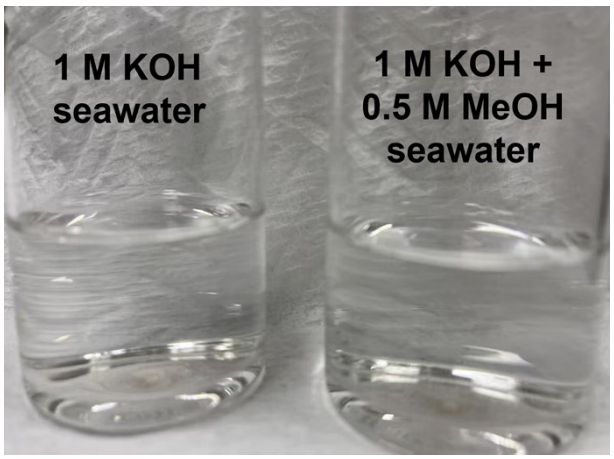

Figure S18. Photos of electrolytes (1 M KOH seawater and 1 M KOH + 0.5 MeOH seawater) for FeNi-LDH/Co-Ni_3S_2 after CP tests (5 h) at 100 mA cm^{-2}.

We used iodine titration to detect hypochlorite (oxidation product of chloride ions) to directly observe chlorine resistance. Iodine titration was performed immediately after stability testing (100 mA cm^{-2} for 5 h in 1 M KOH seawater and 1 M KOH + 0.5 MeOH seawater, respectively). 20 mL of electrolyte was placed into a bottle, and 15 mL of freshly prepared 0.5 M KI solution was added under magnetic stirring. The electrolyte did not turn yellow because there was no or very little hypochlorite in the solution to oxidize I^- to I_2. In other words, the less hypochlorite, the clearer the solution.

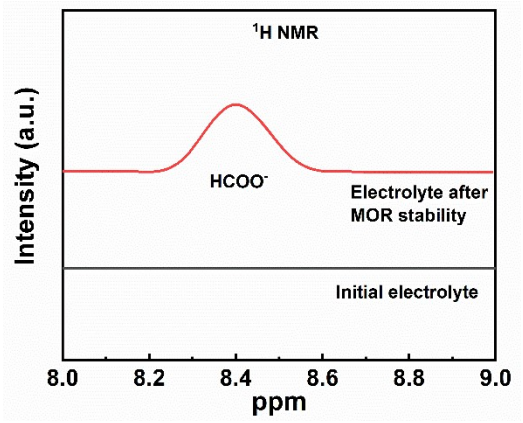

Figure S19. ^{1}H NMR analysis of anodic formate production from methanol.

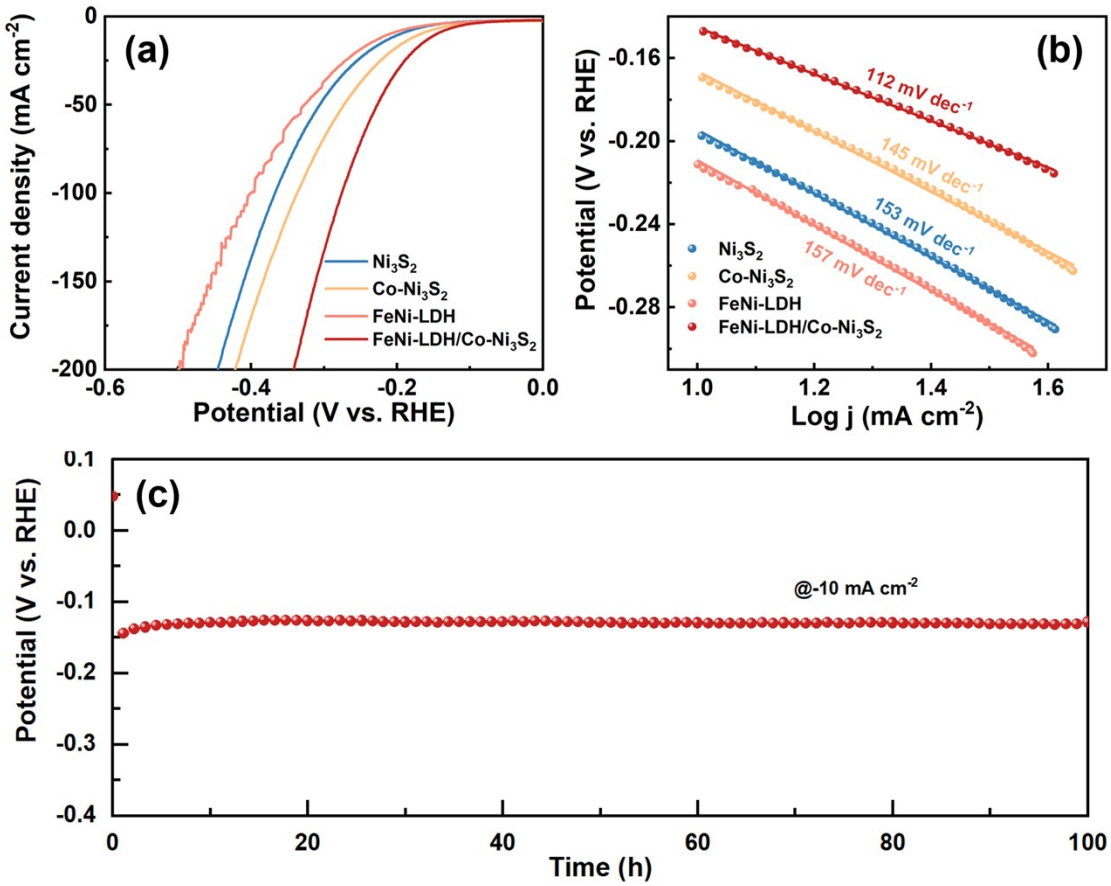

Figure S20. HER performances in 1M KOH. (a) LSV curves; (b) Tafel slopes; (c) Stability of FeNi-LDH/Co-Ni_3S_2 at a current density of -10 mA cm^{-2}.

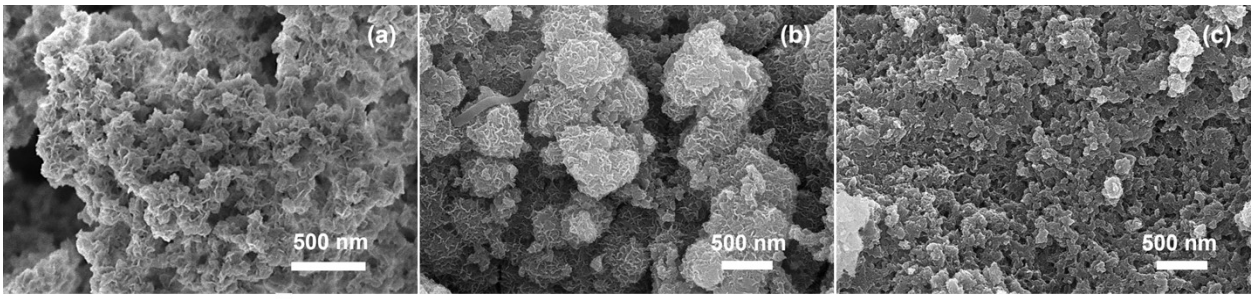

Figure S21. FE-SEM image of FeNi-LDH/Co-Ni_3S_2 after OER stability test. (a) 10 mA cm^{-2} in 1 M KOH + seawater electrolyte for 100 h; (b) 500 mA cm^{-2} in 1 M KOH + seawater electrolyte for 500 h; (c) 500 mA cm^{-2} in 6 M KOH + seawater electrolyte for 120 h.

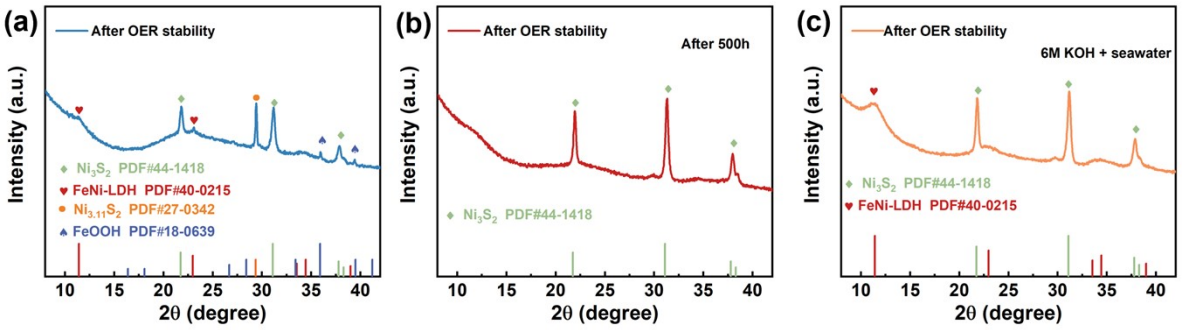

Figure S22. XRD pattern of FeNi-LDH/Co-Ni_3S_2 after OER stability test. (a) 10 mA cm^{-2} in 1 M KOH + seawater electrolyte for 100 h; (b) 500 mA cm^{-2} in 1 M KOH + seawater electrolyte for 500 h; (c) 500 mA cm^{-2} in 6 M KOH + seawater electrolyte for 120 h.

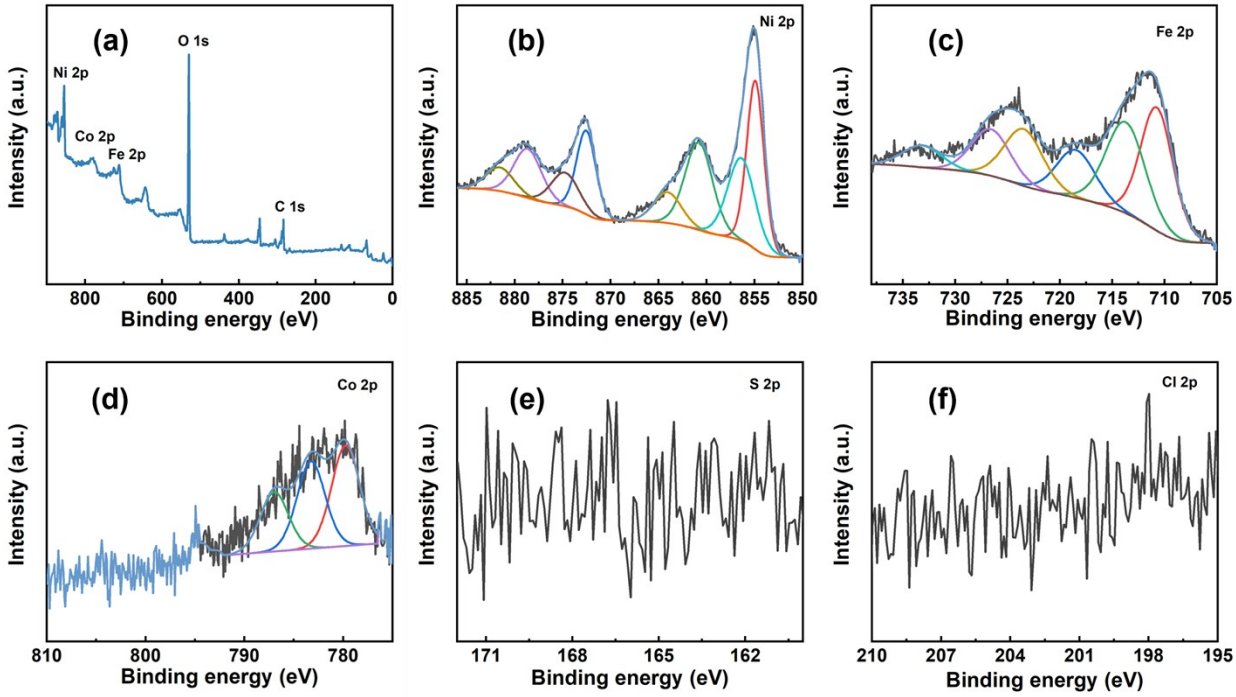

Figure S23. (a) XPS survey spectra. High-resolution (b) Ni 2p, (c) Fe 2p, (d) Co 2p, (e) S 2p, and (f) Cl 2p XPS spectra of FeNi-LDH/Co-Ni_3S_2 after OER stability at a current density of 10 mA cm^{-2} for 100 h in 1 M KOH + seawater electrolyte.

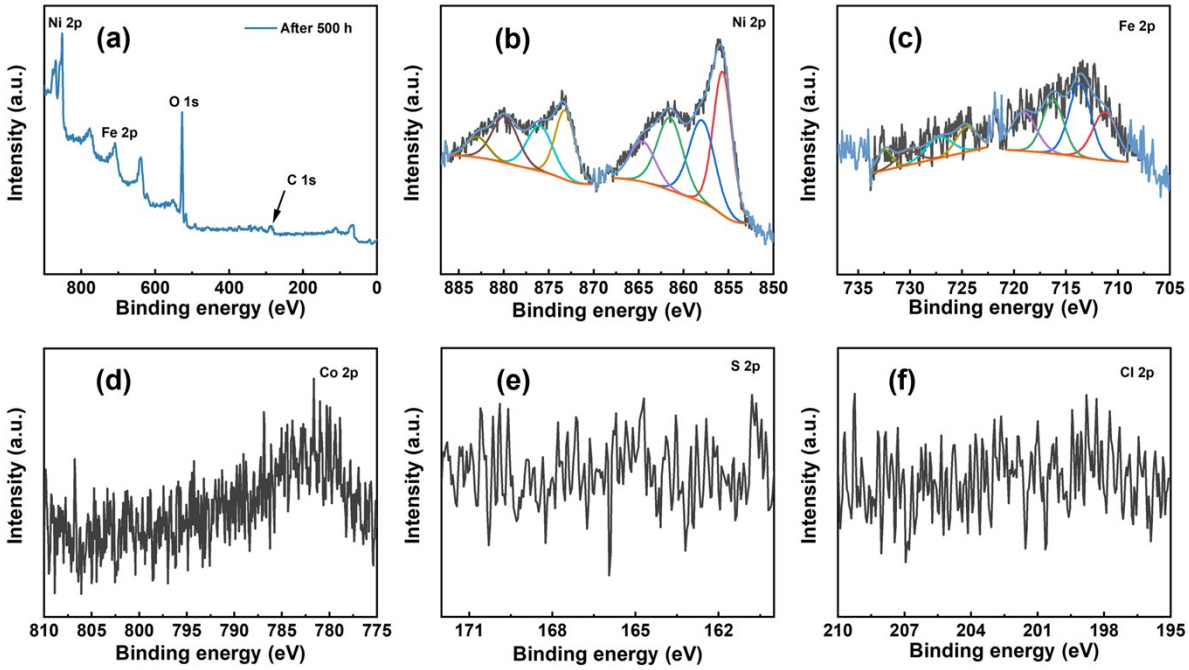

Figure S24. (a) XPS survey spectra. High-resolution (b) Ni 2p, (c) Fe 2p, (d) Co 2p, (e) S 2p, and (f) Cl 2p XPS spectra of FeNi-LDH/Co-Ni_3S_2 after OER stability at a current density of 500 mA cm^{-2} for 500 h in 1 M KOH + seawater electrolyte.

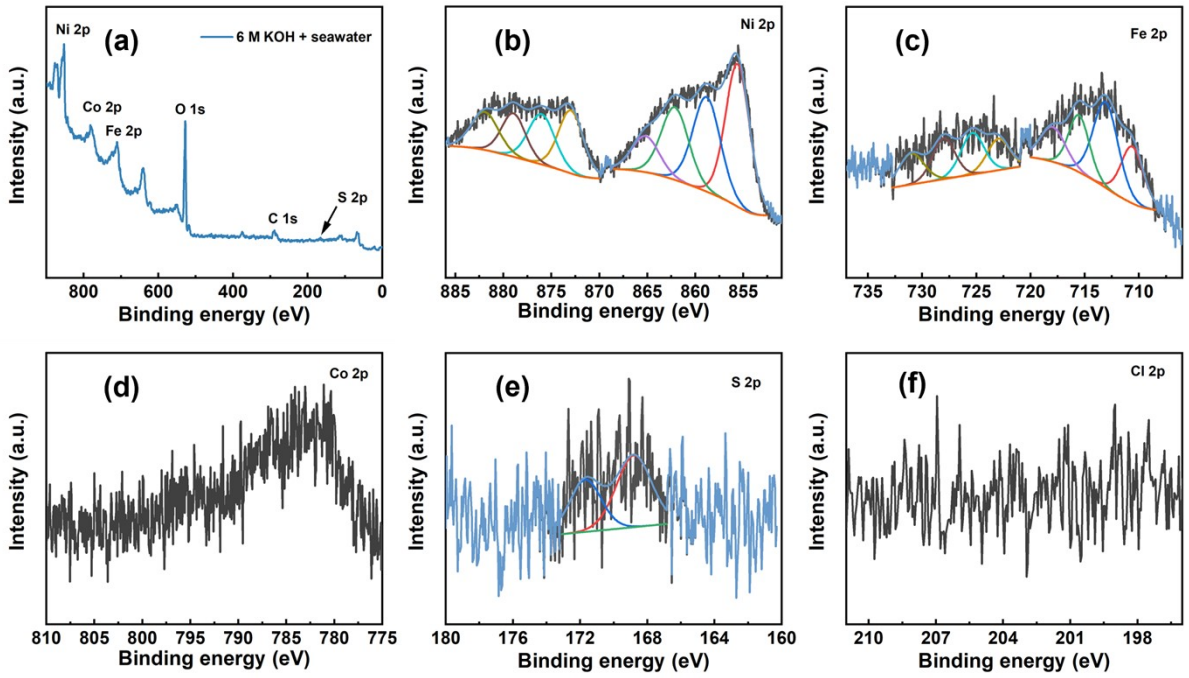

Figure S25. (a) XPS survey spectra. High-resolution (b) Ni 2p, (c) Fe 2p, (d) Co 2p, (e) S 2p, and (f) Cl 2p XPS spectra of FeNi-LDH/Co-Ni_3S_2 after OER stability at a current density of 500 mA cm^{-2} for 120 h in 6 M KOH + seawater electrolyte.

References

1. M.P. Jian, B. Liu, R.P. Liu, J.H. Qu, H.T. Wang, X.W. Zhang, Rsc Adv, 2015, **5**, 48433-48441.
2. C.H. Liang, X.D. Zhang, P. Feng, H.X. Chai, Y.M. Huang, Chemical Engineering Journal, 2018, **344**, 95-104.
3. E. Scavetta, A. Mignani, D. Prandstraller, D. Tonelli, Chem Mater, 2007, **19**, 4523-4529.
4. K. Jiang, W. Liu, W. Lai, M. Wang, Q. Li, Z. Wang, J. Yuan, Y. Deng, J. Bao, H. Ji, Inorganic chemistry, 2021, **60**, 17371-17378.
5. H. Wang, L. Chen, L. Tan, X. Liu, Y. Wen, W. Hou, T. Zhan, Journal of Colloid and Interface Science, 2022, **613**, 349-357.
6. G. Dong, F. Xie, F. Kou, T. Chen, F. Wang, Y. Zhou, K. Wu, S. Du, M. Fang, J. Ho, Materials Today Energy, 2021, **22**, 100883.
7. M. Xiao, C. Wu, J. Zhu, C. Zhang, Y. Li, J. Lyu, W. Zeng, H. Li, L. Chen, S. Mu, Nano Research, 2023, **16**, 8945-8952.
8. Y. Bao, Z. Wu, B. Liu, K. Zhong, M. Guo, J. Tu, B. Wang, X. Lai, ACS Applied Nano Materials, 2023, **6**, 4360-4369.
9. W. Ou, W. Zhang, H. Qin, W. Zhou, Y. Tang, Q. Gao, Journal of Colloid and Interface Science, 2024, **655**, 852-862.
10. Q. Dai, X. He, Y. Yao, K. Dong, X. Liu, X. Guo, J. Chen, X. Fan, D. Zheng, Y. Luo, S. Sun, L. Li, W. Chu, A. Farouk, M. Hamdy, X. Sun, B. Tang, Nano Research, 2024, **17**, 6820-6825.

11. R. Kalusulingam, M. Mariyaselvakumar, S. Mathi, S. Arokiasamy, T. Mikhailova, G. Alexandrovich, I. Pankov, A. Jeffery, T. Myasoedova, Journal of Alloys and Compounds, 2024, **1002**, 175389.

12. L. Wu, L. Yu, Q. Zhu, B. McElhenny, F. Zhang, C. Wu, X. Xing, J. Bao, S. Chen, Z. Ren, Nano Energy, 2021, **83**, 105838.

13. Z. Li, M. Liu, J. Yan, L. Lee, Chemical Engineering Journal, 2023, **473**, 145293.